Angle effect in laser nanopatterning with particle-mask

Z. B. Wang, M. H. Hong, B. S. Luk'yanchuk, Y. Lin, Q. F. Wang et al.

Citation: J. Appl. Phys. **96**, 6845 (2004); doi: 10.1063/1.1786652
View online: http://dx.doi.org/10.1063/1.1786652
View Table of Contents: http://jap.aip.org/resource/1/JAPIAU/v96/i11
Published by the AIP Publishing LLC.

Angle effect in laser nanopatterning with particle-mask

Z. B. Wang and M. H. Hong[a)]
Data Storage Institute, DSI Building, 5 Engineering Drive 1, Singapore 117608, Republic of Singapore and Department of Electrical and Computer Engineering, National University of Singapore, Singapore 117576, Republic of Singapore

B. S. Luk'yanchuk
Data Storage Institute, DSI Building, 5 Engineering Drive 1, Singapore 117608, Republic of Singapore

Y. Lin, Q. F. Wang, and T. C. Chong
Data Storage Institute, DSI Building, 5 Engineering Drive 1, Singapore 117608, Republic of Singapore and Department of Electrical and Computer Engineering, National University of Singapore, Singapore 117576, Republic of Singapore

(Received 22 January 2004; accepted 29 June 2004)

Parallel nanostructuring of substrate surface with particle-mask is a promising technology that may significantly improve the patterning speed under single laser pulse irradiation. In this paper, the influence of the incidence wave angle on the pattern structures is investigated. Polystyrene spherical particles were deposited on the surface in a monolayer form by self-assembly. The sample was then irradiated with 248 nm KrF laser at different incidence angles α. It is found that nanostructures can be formed at different positions with different incidence angles. Both round-shape and comet-shape nanostructures can be produced. By varying the incidence angles, the depth of the nanostructures can also be controlled. To explain the different nanostructures produced at different angles, the intensity field distributions under the particle were calculated according to an exact model for light scattering by a sphere on the substrate (P. A. Bobbert and J. Vlieger, Physica A **137A**, 209 1986). The main equation in the original model was reformed for the ease of numerical simulation. A method was proposed to calculate the total electric and magnetic field as an extension to the model. The theoretical results are in good agreement with the experimental results. © *2004 American Institute of Physics*. [DOI: 10.1063/1.1786652]

I. INTRODUCTION

Laser-induced near-field patterning of surface at a resolution far below the diffraction limit has attracted more and more attention in recent years due to its extensive potential applications in high-density data storage and high-resolution optical lithography for nanodevice fabrication.[1] In most near-field techniques, the subwavelength resolution is achieved by placing a small aperture between the recording medium and light source. If the aperture-to-medium separation is controlled at a distance much smaller than the wavelength, the resolution will be determined by the aperture size instead of the diffraction limit.[2] This technique is used in the scanning near-field optical microscope (SNOM) system: a single hollow optical fibre with a small aperture at its end is used to deliver the laser beam.[3] Due to the near-field optical enhancement effect at the tip, the SNOM system is able to perform surface modification in a nanoscale of different kinds of materials. However, this approach is difficult to implement in an industrial application due to sophisticated hardwares to control the near-field distance and low throughout. One promising approach that could lead to massively parallel nanostructuring was demonstrated by using particle-mask to pattern a solid substrate.[4–7] The technique employs a regular two-dimensional (2D) array of microspheres/nanospheres to focus the incident laser radiation onto the substrate. It permits single step surface patterning of thousands or millions submicron holes on the substrate with a single or a few laser shots. The energy conversion efficiency by particle microlens/nanolens is close to 100%, which is significantly higher than that in SNOM system (10^{-4}–10^{-5}).[1] However, all of the previous studies were performed under the normal incidence condition, e.g., the laser beam path is perpendicular to the sample surface. The produced nanostructures are formed at positions where spheres originally located. It would be interesting to see the difference between the nanostructures produced by normal incidence wave and angular incidence wave, as that could allow one to produce different nanostructures and to control the nanostructure positions. In this article, we will show the experimental evidences on the angle effect in laser nanopatterning with the particle-mask. Since the intensity field distribution is responsible for the formation of nanostructures, exact examination of these field distributions is very important. The limitation of most previous studies[4,7] lies in the use of conventional Mie theory for the theoretical modeling, and thus the influence of the substrate on the field distribution is neglected. In this paper, we will calculate the exact field distribution under the particle based on the model developed by Bobbert and Vlieger (hereinafter referred as the BV theory). Some extensions have been made to the BV theory in order to numerically evaluate the total electric and magnetic fields in the optical near field.

Following this section, experimental details and results will be firstly given. After that, the BV theory is summarized

a)Author to whom correspondence should be addressed; electronic mail: hong_minghui@dsi.a-star.edu.sg

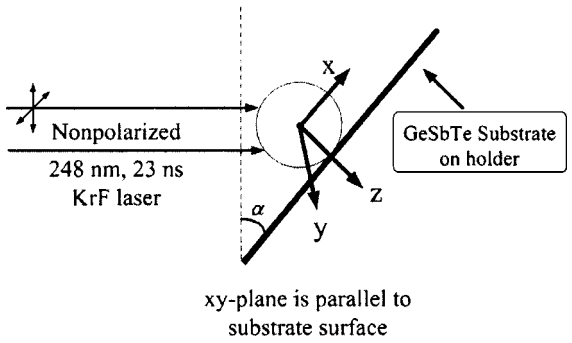

FIG. 1. Schematic showing of experimental setup and choice of coordinate system. *z*-axis is perpendicular to the substrate surface. *x*-axis is along projection direction and *y*-axis is perpendicular to *x*-axis.

and the extensions to the model will be presented in details. Finally, the calculated theoretical pictures are compared with the experimental results.

II. EXPERIMENTAL DETAILS

The sample is a 100 nm-thick $Ge_2Sb_2Te_5$ (GST) film coated on a 0.6 mm polycarbonate substrate. Initial state of the as-deposited film is amorphous. Refractive index of the film is about $1.8049+2.0657\,i$. Melting point of the film is 616 °C. Monodisperse Polystyrene (PS) particles (Duke Scientific Corp.) with a diameter of 1.0 μm were used. They are transparent to ultraviolet (UV) light. Particle suspension was diluted with de-ionized (DI) water and deposited on GST substrate with a dispenser. The sample was then stored inside a refrigerator at 10 °C for 1 h until all the water solvent was evaporated. A KrF excimer pulsed laser ($\lambda=248$ nm, full width at half maximum (FWHM)=23 ns) was used as a light source. The output laser light is nonpolarized and has a rectangular beam shape. A lens of 500 mm focal length focuses laser beam onto the sample mounted on a holder, which is set inside a small vacuum chamber. The holder can be rotated to change the laser incidence angle on the sample surface, as shown in Fig. 1. The intensity incident on the substrate is controlled by placing the sample holder at different focus positions. The minimum spot size is around 10 mm in length and 2 mm in width. With a single pulse irradiation, the damage threshold for the GST sample is around 12.0 mJ/cm^2. Four different incidence angles were examined in this study, e.g., $\alpha=0°$, $\alpha=30°$, $\alpha=45°$, and $\alpha=60°$. The normal incidence corresponds to $\alpha=0°$. Different laser fluences were used to study the laser energy dependence of the nanostructures formed on GST material. The GST surface after the laser nanostructuring was characterized by a scanning electron microscopy (SEM: Hitachi S4100) and the depths were measured by an atomic force microscopy (AFM: Nanoscope D5100).

III. RESULTS AND DISCUSSIONS

A. SEM and AFM results

In the experiments, it is found that most of the PS particles are removed from the substrate surface at normal incidence. As the incidence angle increases, a higher percentage of the particles are left on the sample surface. For 1.0 μm particles, they are attracted to the surface by van der Waals force, which occurs due to dipole interactions. The particles are removed from the GST substrate surface due to the thermal deformation force and/or the ablative force exceeding the particle-surface adhesion force.[8] At different incidence angles, the substrate thermal deformation could result in different "lifting effects" of the particles, which significantly affect the intensity field distributions around the particle.[8] In the following, we describe the experimental results in two parts: First, the patterns formed under the removed particles will be given, and then the patterns formed around the unremoved particles at different incidence angles will be presented.

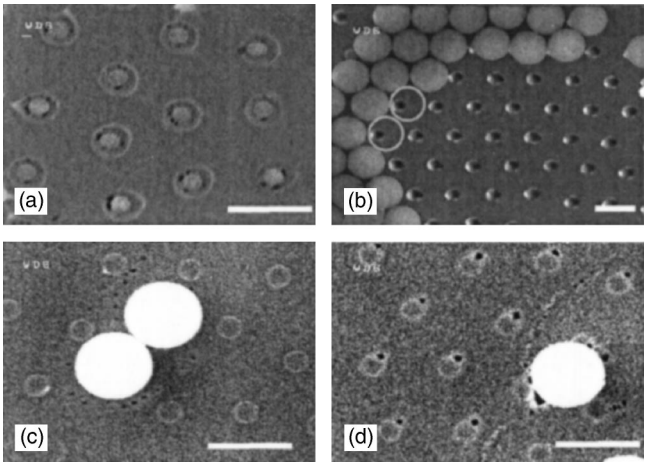

FIG. 2. SEM images of nanodent structures formed on the GST film under the removed particles after one laser pulse irradiation at different incidence angles of (a) $\alpha=0°$, (b) $\alpha=30°$, (c) $\alpha=45°$ and (d) $\alpha=60°$, respectively. Laser fluence is 7.5 mJ/cm^2. Scale bar is 1.0 μm.

Figure 2 shows the SEM images of nanodent structures formed on the GST film under the removed particles after one laser pulse irradiation at a laser fluence of 7.5 mJ/cm^2 and at different incidence angles of (a) $\alpha=0°$, (b) $\alpha=30°$, (c) $\alpha=45°$, and (d) $\alpha=60°$, respectively. At normal incidence, one can see from Fig. 2(a) that the formation of sombrero-shape bumps with an outer rim under the removed spheres. The 3D AFM profile and 2D depth profile of this nanostructure are shown in Fig. 3(a) and 3(b), respectively. The height of the outer rim and the center bump are about 35 nm. The formation of such nanostructure is related to the surface tension gradients caused by the inhomogeneous temperature distribution within the heated layer.[9,10] It leads to Marangoni convection (thermocapillary effect). When the incidence

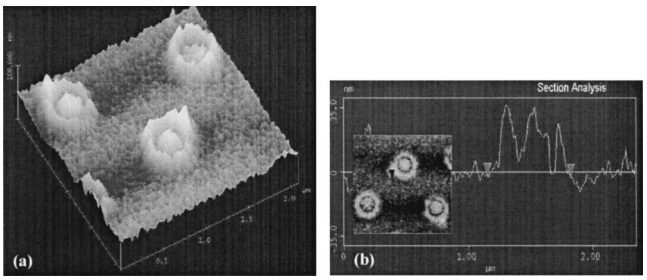

FIG. 3. 3D AFM image and 2D AFM profile of the nanodent structure in Fig. 1(a).

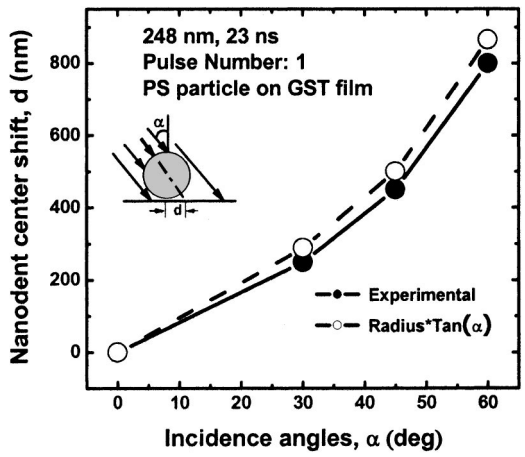

FIG. 4. Dependence of nanodent center shift distance on incidence angle. The solid line represents experimental data and the dashed line represents the calculated value of $Radius \times tan(\alpha)$ from the conventional geometrical optics.

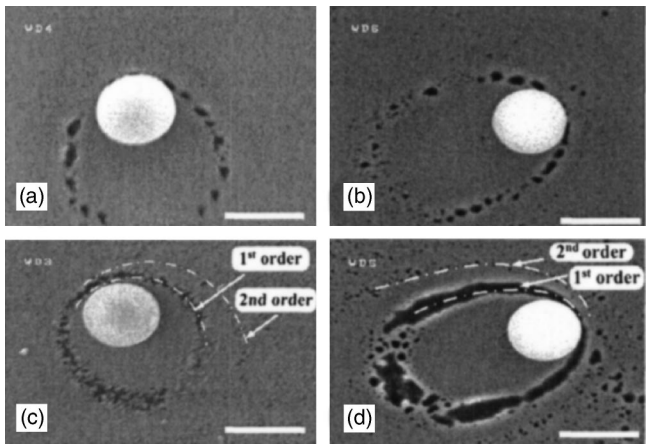

FIG. 5. SEM images of comet-shape patterns formed on GST film around un-removed particles at different angles and laser fluences, (a) $\alpha=45°$, 7.5 mJ/cm^2, (b) $\alpha=60°$, 7.5 mJ/cm^2, (c) $\alpha=45°$, 10.5 mJ/cm^2, and (d) $\alpha=60°$, 10.5 mJ/cm^2. The dashed lines show the different orders of the rings. Scale bar is 1.0 μm.

angle increases to 30°, we found that sombrero-shape structures disappear and "clean" bowl-shape nanodents can be obtained [Fig. 2(b)]. As we have shown previously that the nanodents change their shapes at different laser energies at the normal incidence for the GST material: bowl-shape nanodents at low laser fluences and sombrero-shape nanodents at high laser fluences.[9] The formation of the bowl-shape nanodents at 30° in present study, therefore, indicates the intensity field under the particle is lower than that in the normal incidence case. The depths of the bowl-shape nanodents are around 50 nm. On the other hand, the center locations of these nanostructures are found to be shifted from the contacting point to a position around 250 nm away, as indicated by the circle mark in Fig. 2(b). When the incidence angle increases to 45°, it is found that the bowl-shape nanodents become shallower with a depth around 40 nm [Fig. 2(c)]. The centers of these nanodents are shifted from the contacting point to a position around 450 nm away. As angle increases further to 60°, the depth of the nanodents decreases to around 20 nm and the center shifted from the contacting point to a further position around 800 nm away. Interestingly, it is observed that Fig. 2(d) is different from Fig. 2(c) with the formation of a 50 nm-diameter hole at the edge of each bowl-shape nanodent. As will be shown below, this is because of the asymmetry intensity field distribution on the substrate surface at 60° incidence. Figure 4 summarizes the measured nanodent center shift distance at different incidence angles. As can be seen, the experimental data (solid line) are very close to the theoretical values of $Radius \times \tan(\alpha)$ given by geometrical optics (dashed line).

For the unremoved particles, interesting patterns are observed in the surrounding regions at 45° and 60° incidences. Figure 5 shows the SEM images of the patterns formed on the GST film around the unremoved isolated particles at different incidence angles and laser fluences, e.g., (a) $\alpha=45°$, 7.5 mJ/cm^2, (b) $\alpha=60°$, 7.5 mJ/cm^2, (c) $\alpha=45°$, 10.5 mJ/cm^2, and (d) $\alpha=60°$, 10.5 mJ/cm^2, respectively. From Figs. 5(a)–5(d), it can be observed that comet-shape ring patterns are formed around the unremoved particles at 45° and 60° incidences. The particles are stayed on the lobe of the patterns instead of the centers. The patterns are not linked together with some broken fine structures at a laser fluence of 7.5 mJ/cm^2. When the laser fluence increases to 10.5 mJ/cm^2, the broken parts disappear and the patterns are linked together continuously. Meanwhile, the higher-order rings around the particles start to appear at a laser fluence of 10.5 mJ/cm^2. The first ring in Fig. 5(c) corresponds to the ring observed in Fig. 5(a). The absence of these higher-order rings in Fig. 5(a) is due to the insufficient intensity of these rings to induce the patterns on the substrate surface. It is also observed in the experiments that the presences of the neighboring particles affect the comet-shape ring patterns. For many unremoved particles gathering together, the patterns can only be observed around the particles located at the edges. The influences of neighboring particles make the theoretical analysis of the problem complicated. In present study, we will limit the understanding of the intensity field distribution to isolated particles. Near field intensity distributions under the particle based on a "particle-on-substrate" model in an exact form are calculated to explain the experimental results.

B. Theoretical calculation of optical near field around a particle

To examine the optical near field around a small particle, we use the BV theory for light scattering by a sphere on the substrate.[11] BV theory is an extension to the classical Mie theory[12] by including the multiple scattering and reflection processes between substrate and particle. The main governing equation in BV theory is

$$W^S = B(V^I + V^{IR} + V^{SR}), \tag{1}$$

where W^S represents the scattering wave, V^I the incidence wave, V^{IR} the reflected incidence wave, and V^{SR} the reflected scattering wave. The B matrix is exactly same as that in the Mie theory. The V^{SR} wave and W^S wave are linearly related by a matrix A which characterizes the reflection of spherical waves by the substrate,

$$V^{SR} = AW^{S}. \tag{2}$$

From Eqs. (1) and (2), one can find that the formal solution is

$$W^{S} = (1 - BA)^{-1} B(V^{I} + V^{IR}). \tag{3}$$

Thus, the technical problem is related to the calculation of the "scattering reflection matrix" A and the inverse matrix $(1-BA)^{-1}$ in Eq. (3). The A matrix is obtained from the generalization of Weyl integration method by which the spherical scattering W^S wave is expressed as an integral over plane waves traveling into various directions:[11]

$$A_{l',m',f',l,m,f} = i^{l'-1}\sqrt{\frac{2l'+1}{l'(l'+1)}}(-1)^{m-1}\delta_{mm'} \times \int_{0}^{\pi/2-i\infty} \sin\alpha \, d\alpha \, e^{2i\, q\cos\alpha} a^{m}_{l',f',l,f}(\alpha). \tag{4}$$

To the best of our knowledge, the numerical evaluation of the optical fields based on the BV theory is mainly applied to the far-field scattering problems up to date.[13,14] In the far field, theoretical formula can be significantly simplified due to the fact that radial components (E_r, H_r) of these fields tend to zero, as shown by Bobbert *et al.* and Kim *et al.*[13–15] However, in the near field, the radial component is comparable to the angular components and thus cannot be neglected. Meanwhile, due to the presence of radial components, the reflected scattering wave V^{SR} in the near field cannot be evaluated by the method proposed in the BV theory. As an extension to the BV theory, we propose that the total field in the optical near field can be calculated by constructing the total Debye potentials as

$${}^{f}D(r,\theta,\varphi) = \sum_{l=1}^{\infty}\sum_{m=-l}^{l}\left\{\left[{}^{f}(V_l^m)^{I} + {}^{f}(V_l^m)^{IR} + {}^{f}(V_l^m)^{SR}\right] j_l(kr) + {}^{f}(W_l^m)^{S} h_l^{(1)}(kr)\right\} Y_l^m(\theta,\varphi), \tag{5}$$

where $j_l(\rho) = \sqrt{\pi\rho/2}J_{l+1/2}(\rho)$ and $h_l^{(1)}(\rho) = \sqrt{\pi\rho/2}H_{l+1/2}^{(1)}(\rho)$ are spherical Bessel and Hankel functions, respectively. $Y_l^m(\theta,\varphi)$ is the spherical harmonic of degree l and order m, following the notations in BV theory. The index f in Eq. (5) can be $e({}^{e}D)$ or $h({}^{h}D)$, representing the electric Debye potential and magnetic Debye potential, respectively. In the BV theory, an idea is given for the evaluation of ${}^{f}(V_l^m)^{SR}$ matrix: First, one should calculate the scattering electric and magnetic fields from Eqs. (1)–(4) and consequently repeat the Weyl integration to decompose the scattering field into plane waves to calculate the reflection scattering field. This method requires the calculation of A matrix in a complete form, which involves all possible orders of (l,m) and (l',m'). Although the idea is clear, developing numerical program fulfilling it seems rather difficult: (1) the calculation time is extended by a factor of $l' \times (2l'+1)$ and (2) l' should be truncated at an appropriate order to ensure the convergence conditions. To overcome this problem, here we propose a method to compute ${}^{f}(V_l^m)^{SR}$ matrix: First, we rewrote Eq. (3) into the following alternative form:

$${}^{e}(W_l^m)^{S} = B_{l',m',e;l,m,e}\left({}^{e}V_l^m - A_{l',m',h;l,m,h}B_{l',m',h;l,m,h}\,{}^{e}V_l^m + A_{l',m',e;l,m,h}B_{l',m',h;l,m,h}\,{}^{h}V_l^m\right)/G_{l',m',l,m}, \tag{6a}$$

$${}^{h}(W_l^m)^{S} = B_{l',m',h;l,m,h}(A_{l',m',h;l,m,e}B_{l',m',e;l,m,e}\,{}^{e}V_l^m - A_{l',m',e;l,m,e}B_{l',m',e;l,m,e}\,{}^{h}V_l^m + {}^{h}V_l^m)/G_{l',m',l,m}, \tag{6b}$$

where

$$G_{l',m',l,m} = 1 - (A_{l',m',h;l,m,h} + A_{l',m',e;l,m,h}A_{l',m',h;l,m,e}B_{l',m',e;l,m,e}) \times B_{l',m',h;l,m,h} + A_{l',m',e;l,m,e}B_{l',m',e;l,m,e}(A_{l',m',h;l,m,h} \times B_{l',m',h;l,m,h} - 1) \tag{6c}$$

and

$${}^{e}V_l^m = {}^{e}(V_l^m)^{I} + {}^{e}(V_l^m)^{IR}, \quad {}^{h}V_l^m = {}^{h}(V_l^m)^{I} + {}^{h}(V_l^m)^{IR} \tag{6d}$$

In practice, we found that such reformation is beneficial for programming and more efficient in term of calculation speed since it does not involve further operation of matrix inversion. After we get ${}^{S}W$ matrix, the ${}^{f}(V_l^m)^{SR}$ matrix will be calculated by

$${}^{f}(V_l^m)^{SR} = \frac{{}^{f}(W_l^m)^{S}}{{}^{f}B_l^m} - {}^{f}(V_l^m)^{I} - {}^{f}(V_l^m)^{IR}. \tag{7}$$

Since ${}^{f}(W_l^m)^{S}$ matrix has a simplified form (l',m' orders are limited to $l'=l, m'=m$) due to the presence of KroneckDelta functions $\delta_{l,l'}$, $\delta_{m,m'}$ in the B matrix, there is no requirement to calculate all possible orders of (l,m) and (l',m'). Applying this method, Eq. (5) can be simplified as

$${}^{f}D(r,\theta,\varphi) = \sum_{l=1}^{\infty}\sum_{m=-l}^{l}\left\{\left[\frac{{}^{f}(W_l^m)^{S}}{{}^{f}B_l^m}\right] j_l(kr) + {}^{f}(W_l^m)^{S} h_l^{(1)}(kr)\right\} Y_l^m(\theta,\varphi) \tag{8}$$

Finally, the total electric and magnetic field components [spherical coordinate (r,θ,φ)] can be calculated from the scalar Debye potentials by

$$E_r = \left(\frac{\partial^2}{\partial r^2} + k^2\right)(r\,{}^{e}D), \tag{9a}$$

$$E_\theta = \frac{1}{r}\frac{\partial^2}{\partial\theta\partial r}(r\,{}^{e}D) + \frac{ik}{r\,\sin\theta}\frac{\partial}{\partial\varphi}(r\,{}^{h}D), \tag{9b}$$

$$E_\varphi = \frac{1}{r\,\sin\theta}\frac{\partial^2}{\partial\varphi\partial r}(r\,{}^{e}D) - \frac{ik}{r}\frac{\partial}{\partial\theta}(r\,{}^{h}D), \tag{9c}$$

$$H_r = \left(\frac{\partial^2}{\partial r^2} + k^2\right)(r\,{}^{h}D), \tag{9d}$$

$$H_\theta = \frac{1}{r}\frac{\partial^2}{\partial\theta\partial r}(r\,{}^{h}D) - \frac{ik}{r\,\sin\theta}\frac{\partial}{\partial\varphi}(r\,{}^{e}D), \tag{9e}$$

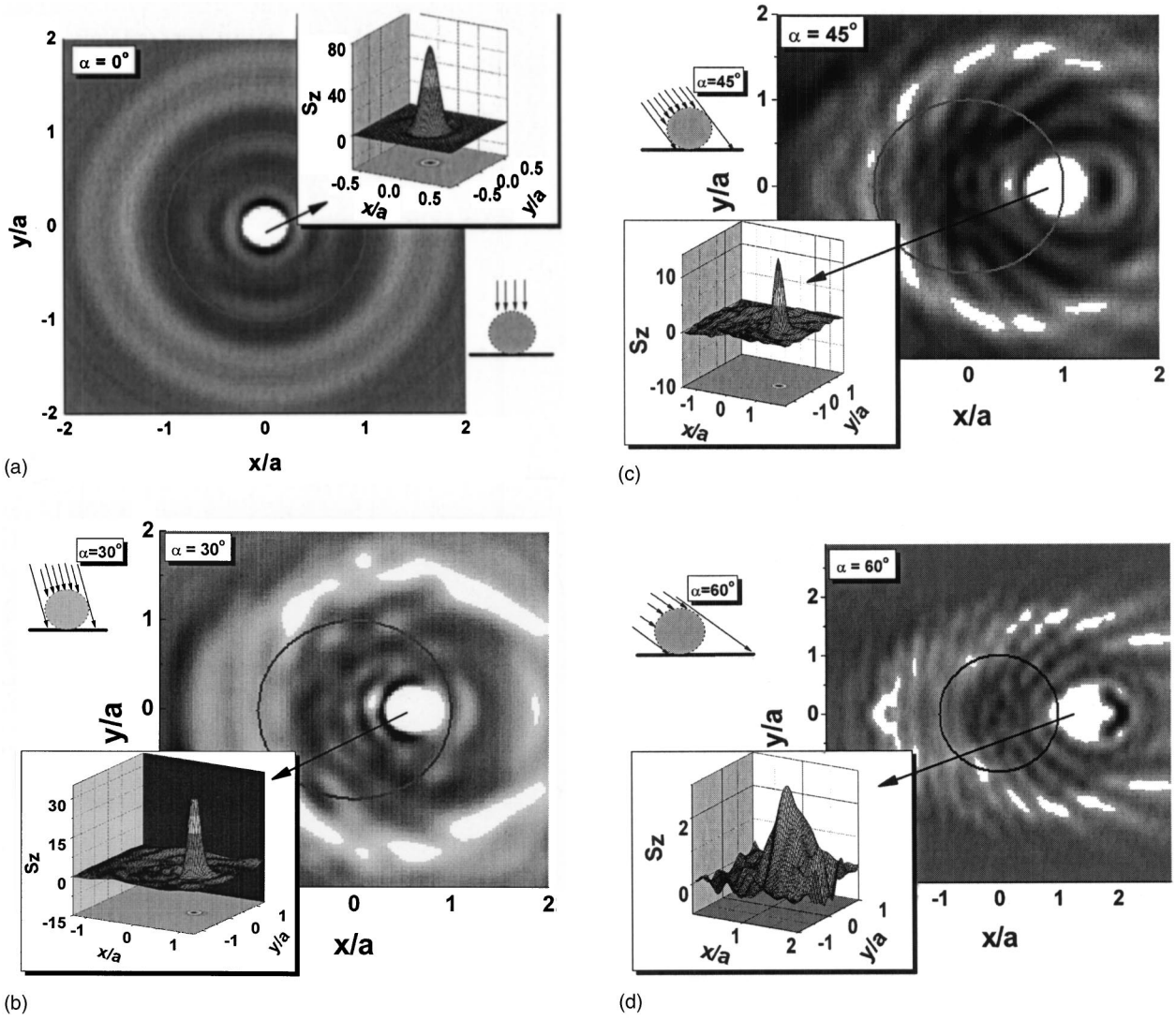

FIG. 6. Calculated intensity field ($I=S_z$) distribution under 1.0 μm PS particles at different incidence angles of (a) $\alpha=0°$, (b) $\alpha=30°$, (c) $\alpha=45°$, and (d) $\alpha=60°$, respectively. The white color represents the areas where the intensity field exceeding the material damage threshold 12.0 mJ/cm^2. Surface thermal deformation is neglected.

$$H_\varphi = \frac{1}{r\ \sin\theta}\frac{\partial^2}{\partial\varphi\partial r}(r^h D) + \frac{ik}{r}\frac{\partial}{\partial\theta}(r^e D). \tag{9f}$$

A computer program was written incorporating the aforementioned BV theory. The required spherical Bessel and Hankel functions for arbitrary orders are evaluated using the technique presented by Germer,[15] e.g., recursion relationships for the low orders and Taylor series formulization for the high orders. This special technique is necessary for the problems involving orders much higher than the conventional truncating order ($l_{\max}=x+4x^{1/3}+2$).[16] The required spherical harmonic functions are evaluated using derived recursion formula based on the associated Legendre function recursion relationships presented by Press *et al.*[17] To ensure the convergence conditions in Eqs. (6a) and (6b), the A matrix is firstly calculated for orders much larger than $x+4x^{1/3}+2$, and consequently use parts of them for smaller $l_{\max}$. The angle effect parameters, such as the light incidence angle (α) and the polarization direction (β) are taken into account by the ${}^fV_l^m(\alpha,\beta,\gamma)^I$ and ${}^fV_l^m(\alpha,\beta,\gamma)^{IR}$ functions in Eq. (6d). Since the laser source is nonpolarized in this study, the final near-field intensity field[9,18] $I=S_z$ (z-component of the Poynting vector) could be considered as the total of the intensity fields calculated for polarization angles of $\beta=0°$ (half-intensity p-polarized component) and $\beta=90°$ (half-intensity s-polarized component). In the following, theoretical figures are presented and compared with experimental results.

Figure 6 shows the calculated intensity field ($I=S_z$) distribution under 1.0 μm PS particles at different incidence angles of (a) $\alpha=0°$, (b) $\alpha=30°$, (c) $\alpha=45°$, and (d) $\alpha=60°$, respectively. In these plots, the white color scale represents the areas where the intensity field exceeding the material damage threshold 12.0 mJ/cm^2 (corresponding to an intensity enhancement factor of 1.6). To explain the experimental results in Figs. 2(a)–2(d), the theoretical intensity peak values and corresponding peak positions are summarized in Table I.

From Table I, one can see that the peak value decreases quickly as incidence angle increases, from 33.07 at 30° incidence to 3.59 at 60° incidence. This could explain (the presence of neighboring particles could affect the intensity field)

TABLE I. Normalized peak enhancement and peak position at different angles.

Angles (deg)	Peak enhancement factor (normalized)	Peak position (nm)
$\alpha=0°$	70.48	(X:0, Y:0)
$\alpha=30°$	33.07	(X: 270, Y:0)
$\alpha=45°$	13.13	(X: 435, Y:0)
$\alpha=60°$	3.59	(X: 635, Y:0)

why the nanodent structures become shallower as incidence angle increases from 30° to 60° in Figs. 2(b)–2(d). It can also be seen clearly from the insets in Figs. 6(a)–6(d) that the nanodents are formed at some positions shifted from the contacting point. It should be noted that at $\alpha=0°$, $\alpha=30°$, and $\alpha=45°$ the theoretical peak positions are in coincidence with the nanodent center positions as observed in the experiment. The intensity distribution profiles are uniform and symmetric with respect to the peak positions. However, for $\alpha=60°$ one can see from Table I and Fig. 6(d) inset that the intensity distribution profile becomes asymmetric and nonuniform with respect to the nanodent center. The peak intensity is not at the nanodent center but at a position shifted closer to the contacting point, which corresponds to the 50 nm hole observed at the edge of each bowl-shape nanodent in Fig. 2(d).

From the intensity contour plots in Figs. 6(a)–6(d), one can see the complex intensity field distribution under the particle after multiple scattering and reflection processes between substrate and particle. At $\alpha=45°$ and $\alpha=60°$, the calculated results are in a good agreement with experimental results, comet-shape ring patterns formed at 45° and 60° incidences. We found that the projection directions of these patterns are governed by the *p*-polarized component in the incidence light (contribution of the *s*-polarized component to $I=S_z$ field is minor compared with *p*-polarized component). The multiple ring structures can also be clearly seen in Figs. 6(c) and 6(d). These higher-order rings can be seen at a higher laser fluence, as shown in Figs. 5(c) and 5(d). However, a discrepancy arises for $\alpha=30°$, the intensity contour plot in Fig. 6(b) shows the existence of patterns around unremoved particles while they are not observed in the experiments. We confirm such discrepancy by repeating the experiments for several times. To explain this, we propose that the lifting effect of the particle due to thermal deformation could be the main reason. As shown above, the peak intensity is high at a position close to the contacting point at small incidence angles, which could result in a more pronounced thermal deformation of the substrate surface. Since intensity drops quickly with lifting distance,[8] the comet-shape patterns in Fig. 6(b) for $\alpha=30°$ cannot be seen due to the intensity drops to a level below the material damage threshold. However, more investigations are needed to clarify the discrepancy. On the other hand, the *s*-polarized component of the incident light seems to have a minor influence on the final intensity field $I=S_z$ in this study. Linearly polarized light source should be applied to further clarify the problem.

IV. CONCLUSION

The angle effect in laser nanopatterning with particle-mask is investigated. Two kinds of patterns left on the substrate surface after single laser pulse irradiation: (1) Comet-shape ring nanostructures formed around unremoved particles at 45° and 60° incidence angles and (2) sombrero-shape or bowl-shape nanodent structures formed under removed particles with their positions shifted from the contacting point with a distance around $Radius \times \tan(\alpha)$. The depth of nanodents decreases as incidence angle increases due to the fast decay of maximum intensity field at these spots. The experimental results have been successfully explained by the field intensity distribution profile in optical near field regions of the particle.

ACKNOWLEDGMENTS

The authors wish to thank Ms. Wang Weijie for her valuable discussions and Van Lihui for her support in AFM measurement. Z. B. Wang is thankful to Data Storage Institute for providing the research scholarship.

[1] M. Ohtsu and H. Hori, *Near-field Nano-optics* (Kluwer Academic, New York, 1999).
[2] E. Betzig, J. K. Trautman, R. Wolfe, E. M. Gyorgy, P. L. Finn, M. H. Kryder, and C.-H. Change, Appl. Phys. Lett. **61**, 142 (1992).
[3] S. Patane, A. Arena, M. Allegrini, L. Amdereozzi, M. Faetti, and M. Giordano, Opt. Commun. **210**, 37 (2002).
[4] H.-J. Munzer *et al.*, Proc. SPIE **4426**, 180 (2001).
[5] O. Watanabe, T. Ikawa, M. Hasegawa, M. Tsuchimori, and Y. Kawata, Appl. Phys. Lett. **79**, 1366 (2001).
[6] K. Piglmayer, R. Denk, and D. Bauerle, Appl. Phys. Lett. **80**, 4693 (2002).
[7] Y. Lu, S. Theppakuttai, and S. C. Chen, Appl. Phys. Lett. **82**, 4143–4145 (2003).
[8] Y. W. Zheng, B. S. Luk'yanchuk, Y. F. Lu, W. D. Song, and Z. H. Mai, J. Appl. Phys. **90**, 2135 (2001).
[9] Z. B. Wang, M. H. Hong, B. S. Luk'yanchuk, S. M. Huang, Q. F. Wang, L. P. Shi, and T. C. Chong Appl. Phys. A: Mater. Sci. Process. **79**, 1603 (2004).
[10] Y. Lu and S. C. Chen, Nanotechnology **14**, 505 (2003).
[11] P. A. Bobbert and J. Vlieger, Physica A **137A**, 209 (1986).
[12] G. Mie, Ann. Phys. (Leipzig) **25**, 377 (1908).
[13] P. A. Bobbert, J. Vlieger, and R. Greef, Physica A **137A**, 243 (1986).
[14] J. H. Kim, S. H. Ehrman, G. W. Mulholland, and T. A. Germer, Proc. SPIE **4449**, 281 (2001).
[15] T. A. Germer, 4.00 ed., SCATMECH: Polarized Light Scattering *C++* Class Library (avaliable at http://physics.nist.gov/scatmech), USA, 2003.
[16] C. F. Bohren and D. R. Huffman, *Absorption and Scattering of Light by Small Particles* (Wiley, New York, 1983).
[17] W. H. Press, B. P. Flannery, S. A. Teukolsky, and W. T. Vetterling, *Numerical Recipes: The Art of Scientific Computing* (Cambridge University, Cambridge, England, 1986).
[18] B. S. Luk'yanchuk, N. Arnold, S. M. Huang, Z. B. Wang, and M. H. Hong, Appl. Phys. A: Mater. Sci. Process. **77**, 209 (2003).